KRONOS FUSION ENERGY

PAPER 2.2 · THE KRONOS 2026 SERIES

An Advanced-Fuel Scorecard for D-T, D-D, D-3He and p-11B: Reactivity, Neutron Fraction and Direct-Conversion Trades Behind the Breeder and Burner Fuel Choices

Fuel choice is the most consequential and the most emotionally contested decision in a fusion program: the pull toward the aneutronic ideal routinely overrides the reaction…

Read it live — 3-D model · physics validator · film series

BY P I FORD AND G L KULCINSKI

2026 · EDITORIAL EDITION

THE OFFICIAL RECORD

What this document is, and how to read its numbers

This is a combined editorial. It gathers, in one volume, the two design studies Kronos Fusion Energy released in 2026 — a compact spherical-tokamak tritium/helium-3 breeder and a deuterium–helium-3 tandem-mirror generator — together with the intellectual-property estate, the people, and, in the internal edition, the full commercial case. The scientific text is the same text that appears in the arXiv preprints and the journal submissions; the editorial adds the apparatus a reader needs to hold the whole program at once, and nothing in the physics is altered to fit it.

THE HONESTY STANCE IS THE ASSET

Every headline quantity carries an **evidence class** — DERIVED RECOMPUTED MEASURED REQUIREMENT — and, where a number is a modelled extrapolation rather than a demonstrated value, it is labelled as such and its downside is shown next to it. Several quantities in the underlying corpus moved after first publication; where a value has been withdrawn or restated, the record says so plainly. This is deliberate: a diligence team will find the load-bearing assumptions, so the document surfaces them first.

TWO EDITIONS

This volume is issued in two editions. The **public edition** (light) carries the physics and the design only — no dollar, price, or per-kilogram figure appears anywhere in it. The **internal edition** (dark) adds the economics, the funding architecture, and the defense-commercial analysis, and is marked *Confidential* accordingly; it is not for public distribution. Where the commercial case rests on a modelled assumption rather than a demonstrated one, it is labelled as such and its downside is shown alongside it, on the same terms as the physics.

TITLE	The Kronos Fleet — Hyperion · Aegis · MetroVolt: A Combined Design & Commercialization Study
AUTHOR	Priyanca Ford, Founder & CEO, on behalf of Kronos Fusion Energy
EDITION	2026 Combined Editorial · first issue
COMPANION WORKS	The five-paper arXiv drop — (1) Breeder, (2) Burner, (3) REBCO magnet & tape, (4) Direct Energy Conversion, (5) AI/ML/Quantum control — with matching numbered Zenodo deposits, plus the IOP journal and IAEA-FEC submissions. Patents were filed before the drop.
NAMING	Hyperion = the breeder; Aegis (defense) and MetroVolt (data-center) = one generator in two housings. Internal mode letters (D1, L) do not appear on public surfaces.
STATUS	Conceptual design & simulation study. Nothing herein is a construction commitment.

HOW TO READ THIS VOLUME

The fleet at a glance, and the way its numbers are marked

This volume opens with *Orientation*, presents the five research papers as a bound sequence, and closes with the *Apparatus*. *Foundations* sets out the three general results both machines rest on. *Paper One* is the Hyperion breeder; *Paper Two* the Aegis / MetroVolt generator; *Papers Three, Four and Five* are the enabling science — high-field REBCO magnets and tape, direct energy conversion, and the AI / ML / quantum control stack. A *Digital Twin & 3-D Model* part follows, then the *Environmental* profile. The *Economics* and levelized cost and the *Business Case* and diligence record appear in the internal edition only; the *Simulations* proof record and the Apparatus — patent portfolio, team, limitations, and sources — close both editions.

THE FLEET AT A GLANCE

	HYPERION	AEGIS	METROVOLT
Role	Strategic-isotope foundry	Defense installation power	Campus power
Machine	**Spherical tokamak**	**Tandem mirror**	**Tandem mirror**
Fuel	Deuterium–tritium	Deuterium–helium-3	Deuterium–helium-3
Delivers	Tritium · ^{3}He · 14 MeV n	Resilient installation power	Firm campus power
Physics bar	**Fusion gain only**	Closure (gates named)	Closure + lunar ^{3}He
In the fleet	Breeds the fuel	Proves the generator	Commercial destination

HOW THE NUMBERS ARE MARKED

Every headline quantity carries an evidence class — DERIVED from first principles, RECOMPUTED from raw data, MEASURED in hardware, or a REQUIREMENT yet to be met. Financial figures carry a case label and are confined to the internal (confidential) edition. Values that moved after first publication are shown as withdrawn or restated rather than quietly changed. A capability you can evaluate is one whose limits are on the page.

ABSTRACT

An Advanced-Fuel Scorecard for D-T, D-D, D-3He and p-11B: Reactivity, Neutron Fraction and Direct-Conversion Trades Behind the Breeder and Burner Fuel Choices

Fuel choice is the most consequential and the most emotionally contested decision in a fusion program: the pull toward the aneutronic ideal routinely overrides the reaction physics. We grade the four candidate fuels — deuterium–tritium (D–T), deuterium–deuterium (D–D), deuterium–helium-3 (D–^{3}He), and proton–boron-11 (p–^{11}B) — on one quantitative ruler, deriving each axis from first principles rather than asserting it. Using the Bosch–Hale Maxwellian-reactivity parametrization and the Nevins–Swain p–^{11}B fit, we compute the reactivity ladder $\langle\sigma v\rangle(T)$, the branch-resolved neutron fraction f_n, the ideal-ignition triple product, and the fusion-to-bremsstrahlung ratio across 1–500 keV, and we close the recoverable-power side of the ledger with a direct-energy-conversion (DEC) efficiency. D–T has the highest reactivity at the lowest temperature but is $\approx 80\%$ neutronic and consumes tritium; D–D needs no tritium but is $\approx 66\%$ neutronic (semi-catalyzed) and low-reactivity; D–^{3}He is only $\approx 5.44\%$ neutronic — the neutrons arising entirely from an unavoidable D–D side channel — but requires helium-3 that Earth does not hold in bulk; p–^{11}B is effectively aneutronic ($< 0.2\%$) yet demands the highest temperature, radiates hardest, and has never reached net gain. We then show that the Kronos architecture follows the scorecard rather than the ideal. A first-principles 0-D power balance run on a GPU high-performance-computing (HPC) campaign reproduces the frozen anchors of the Kronos design register: the D–T spherical-tokamak *breeder* ($Q = 3.076$, $P_{\text{fus}} = 85.04$ MW, $I_p = 9.66$ MA, $f_n = 79.7\%$), where the neutron and the bred material *are* the product; and the D–^{3}He tandem-mirror *burner* ($Q_E = 1.318$, $P_{\text{fus}} = 4298.5$ MW, $f_n = 5.44\%$, plug field 26.49 T, DEC efficiency $\eta = 0.49$), where power is the product and neutrons are the liability. A branch-power reconstruction recovers the 5.44% neutron fraction to within 0.01%, and a fuel-mix optimization places the engineering-gain optimum at the same helium-3 fraction that minimizes the neutron burden. The one honest cost of the D–^{3}He choice — fuel availability — is met by the breeder's co-product helium-3 and is otherwise lunar-gated. Every Kronos operating number is a frozen anchor in the de-risking register.

Open-access deposit (code & data, CC BY 4.0): DOI 10.5281/zenodo.22645766 · Zenodo community *kronos_fusion_energy*. Explore it live: interactive 3-D model · physics validator.

Keywords: advanced fusion fuels · deuterium--helium-3 · proton--boron · neutron fraction · reactivity · direct energy conversion · fuel selection · aneutronic fusion

CONTENTS

Table of Contents

NOMENCLATURE

Symbols, units, and the names of things

Q	plasma (fusion) gain, P_{fus}/P_{aux}
Q_E	engineering gain, net electric out / recirculating in
H_{98}	confinement enhancement over the IPB98(y,2) scaling
Z_{eff}	effective ion charge
c_{ee}	electron–electron bremsstrahlung leading coefficient, 2.120022 (exact)
τ_E	energy confinement time
I_p	plasma current
R_0, a	major radius, minor radius
κ, δ	elongation, triangularity
β_N	normalized plasma beta (Troyon-normalized)
TBR	tritium breeding ratio
DEC	direct energy conversion
CF	plant capacity factor (availability)
FOAK / NOAK / BOAK	first / n^{th} / best of a kind
Hyperion	the ST breeder (internal: Mode D2)
Aegis	the generator, defense/installation housing (internal: Mode M)
MetroVolt	the generator, data-center housing (Mode M)

§ 1

Introduction

Every fusion company implicitly selects a fuel, and that selection propagates into every downstream engineering decision: the neutron wall load and therefore the first-wall lifetime; the tritium supply logistics; the ion temperature the confinement scheme must reach; the shielding mass; the activation and waste class; and the conversion strategy from fusion output to delivered energy. The temptation is to argue *toward* a preferred fuel — most often the aneutronic ideal, p–^{11}B — and to treat the reactivity penalty as a detail to be engineered away later. The history of the field cautions against that ordering [9,5]. We instead grade all four candidate fuels on the same axes and let the architecture fall out of the grades.

PRIOR ART

The quantitative backbone of any fuel comparison is the Maxwellian reactivity (T). The evaluated parametrizations of Bosch and Hale [1] remain the standard for D–T, the two D–D branches, and D–^{3}He; for p–^{11}B the Nevins–Swain analytic fit [2] is the long-standing reference, updated by Putvinski *et al.* [3] for revised cross-section data and non-Maxwellian tails, with the first magnetically-confined p–^{11}B fusion measurements reported only recently [4]. The confinement requirements of advanced fuels were quantified by Nevins [5], who showed that the $n\tau_E T$ needed for D–^{3}He ignition exceeds D–T by more than an order of magnitude; Rider [6] established that grossly non-equilibrium schemes cannot escape this penalty because the recirculating power needed to hold a non-Maxwellian distribution exceeds the fusion power. The Lawson criterion itself [7], and its modern re-expression as a progress metric [8], frame the temperature and triple-product cost of each fuel. On the supply side, the lunar-regolith helium-3 resource has been assessed since the 1980s [10]. On the conversion side, direct energy conversion of charged fusion products has a fifty-year lineage in the mirror program [14,15,16], recently revitalised by high-temperature-superconductor mirror experiments [17]. What has been missing is a single, reproducible ledger that scores all four fuels on one ruler and then *binds* the grades to a concrete, frozen two-machine design point.

CONTRIBUTION

This paper makes four contributions. (i) We assemble the scorecard as a set of *computed*, not asserted, axes: the reactivity ladder, the branch-resolved neutron-fraction functional, the ideal-ignition triple product, and the fusion-to-bremsstrahlung ratio, each derived in Section 2 and evaluated in Section 5. (ii) We show that the D–^{3}He neutron fraction is not an intrinsic property of the D–^{3}He reaction — which is strictly aneutronic — but the residue of an unavoidable deuterium–deuterium side channel, and we reconstruct the Kronos burner value $f_n = 5.44\%$ from a four-branch power balance to within 0.01%. (iii) We map the engineering-gain optimum against the neutron burden as a function of fuel-ion mix and demonstrate that the two coincide at the frozen operating point. (iv) We bind the whole analysis to the Kronos two-machine architecture: a D–T spherical-tokamak breeder in which the neutron is the product, and a D–^{3}He tandem-mirror burner in which power is the product [29,31]. All Kronos operating numbers are frozen anchors in the de-risking register [28]; the competitive grades are public reaction physics.

The companion series develops the individual threads referenced here: the strategic-materials platform integrating breeder and burner [29]; the demonstration that the D–^{3}He cycle does not close indigenously and is lunar-gated [30]; the neutron-lean siting budget that audits the parasitic D–D/D–T neutron sources [31]; the recirculation-resolved engineering-gain closure of the burner [32]; RF alpha-channeling to raise the recoverable charged-particle fraction [33]; direct energy conversion of the charged output [34]; the tritium breeding ladder of the breeder [35]; and the medical-isotope mission that monetizes the breeder's 14 MeV neutron [36].

§ 2

Governing equations and the formal scorecard

We fix notation and derive each scorecard axis from the underlying reaction kinetics. Temperatures are in keV, densities in $\mathrm{m^{-3}}$, reactivities in $\mathrm{m^3\,s^{-1}}$, and power densities in $\mathrm{W\,m^{-3}}$. We assume Maxwellian ion distributions throughout; the non-Maxwellian corrections relevant to p–^{11}B are discussed as a bound in Section 6.

MAXWELLIAN REACTIVITY

For a binary reaction between species a and b with relative velocity v and centre-of-mass (CM) energy $E = \frac{1}{2}\mu v^2$ (μ the reduced mass), the thermal reaction rate per unit volume is $R_{ab} = \frac{n_a n_b}{1+\delta_{ab}} \langle\sigma v\rangle_{ab}$, where the Kronecker delta removes the double count for identical reactants and the Maxwellian-averaged reactivity is the fold of the CM cross-section $\sigma(E)$ over a Maxwell–Boltzmann distribution of relative energies,

$$\langle\sigma v\rangle_{ab}(T) = \left(\frac{8}{\pi\mu}\right)^{1/2} \frac{1}{(k_B T)^{3/2}} \int_0^\infty \sigma(E)\, E\, \exp\left(-\frac{E}{k_B T}\right) \mathrm{d}E.$$

Charged-particle fusion cross-sections are dominated at sub-barrier energies by quantum tunnelling, which is factored out through the astrophysical S-factor,

$$\sigma(E) = \frac{S(E)}{E} \exp\left(-\sqrt{\frac{E_G}{E}}\right), \qquad E_G = (\pi\alpha Z_a Z_b)^2 2\mu c^2 \equiv B_G^2,$$

with α the fine-structure constant, $Z_{a,b}$ the reactant charges, and B_G (in $\mathrm{keV}^{1/2}$) the Gamow constant. Substituting Eq. 2 into Eq. 1 and expanding about the Gamow-peak saddle point yields the Bosch–Hale rational-function parametrization used here [1],

$$\theta(T) = \frac{T}{1 - \dfrac{T\,(C_2 + T\,(C_4 + T\,C_6))}{1 + T\,(C_3 + T\,(C_5 + T\,C_7))}}, \qquad \xi(T) = \left(\frac{B_G^2}{4\,\theta}\right)^{1/3},$$

$$\langle\sigma v\rangle(T) = C_1\,\theta \sqrt{\frac{\xi}{m_r c^2\, T^3}}\, \exp(-3\,\xi),$$

where $m_r c^2$ is the reduced-mass energy and $\{C_1, \ldots, C_7\}$ are the tabulated coefficients for each channel. Equation 3 reproduces the underlying R-matrix evaluations to $\lesssim 0.3\%$ over its stated validity range and is the kernel we evaluate for D–T, D(d,p)T, D$(d,n)^3$He and ^{3}He$(d,p)^4$He. For p–^{11}B the resonance at $E_r \approx 148$ keV forbids a single rational fit; we use the Nevins–Swain decomposition [2]

$$\langle\sigma v\rangle_{p^{11}B}(T) = \underbrace{P_1\,\theta \sqrt{\frac{\xi}{m_r c^2\, T^3}}\, e^{-3\xi}}_{\text{non-resonant}} + \underbrace{A_r\, T^{-3/2} \exp(-E_r/T)}_{\text{resonant}},$$

with $A_r = 5.41 \times 10^{-21}\,\mathrm{m^3\,s^{-1}\,keV^{3/2}}$ and $E_r = 148\,\mathrm{keV}$.

FUSION POWER DENSITY AND THE NEUTRON-FRACTION FUNCTIONAL

The total fusion power density of a multi-species plasma is the sum over reaction channels r,

$$P_{\text{fus}} = \sum_r \frac{n_{a_r} n_{b_r}}{1 + \delta_{a_r b_r}} \langle\sigma v\rangle_r(T)\, Q_r,$$

where Q_r is the reaction Q-value. The scorecard's decisive axis is the fraction of that power carried by neutrons,

$$\boxed{f_n \equiv \frac{P_n}{P_{\text{fus}}} = \frac{\sum_r \frac{n_{a_r} n_{b_r}}{1 + \delta_{a_r b_r}} \langle\sigma v\rangle_r\, \varphi_r\, Q_r}{\sum_r \frac{n_{a_r} n_{b_r}}{1 + \delta_{a_r b_r}} \langle\sigma v\rangle_r\, Q_r}}$$

with $\varphi_r = E_{n,r}/Q_r$ the neutron-energy branching ratio of channel r ($\varphi_r = 0$ for aneutronic channels). For the two-body reactions of interest, momentum conservation fixes φ_r exactly: $\varphi_{\rm DT} = E_n/Q = 14.07/17.59 = 0.800$ and $\varphi_{\rm DDn} = 2.45/3.27 = 0.749$.

D–T (breeder). With only the single channel $\mathrm{D}+\mathrm{T}\to n+\alpha$, Eq. 6 collapses to $f_n = \varphi_{\rm DT} = 0.80$: four-fifths of the yield is a 14 MeV neutron. In the breeder that is not a defect but the point.

D–D (semi-catalyzed). Pure deuterium burns through two nearly equiprobable branches, $\mathrm{D}+\mathrm{D}\to p+\mathrm{T}$ ($Q = 4.03$ MeV) and $\mathrm{D}+\mathrm{D}\to n+{}^3\mathrm{He}$ ($Q = 3.27$ MeV). If the bred tritium is burned in situ ($\mathrm{T}+\mathrm{D}\to n+\alpha$) while the bred helium-3 is extracted as product — the physically relevant "semi-catalyzed" accounting when ^{3}He is monetized — Eq. 6 gives

$$f_n^{\text{D-D}} = \frac{\varphi_{\rm DDn}Q_{\rm DDn} + \varphi_{\rm DT}Q_{\rm DT}}{Q_{\rm DDp} + Q_{\rm DDn} + Q_{\rm DT}} = \frac{2.45 + 14.07}{4.03 + 3.27 + 17.59} = 0.664,$$

i.e. $\approx 66\%$: tritium suppression buys little because the bred tritium reintroduces the 14 MeV line.

D–^{3}He (burner). The primary channel $\mathrm{D}+{}^3\mathrm{He}\to p+\alpha$ ($Q = 18.3$ MeV) is strictly aneutronic ($\varphi = 0$). Neutrons appear only because deuterium reacts with itself. Writing the fuel-ion mix as $x = n_{^3\rm He}/(n_D + n_{^3\rm He})$ so that $n_D = (1-x)n_i$ and $n_{^3\rm He} = x\,n_i$, the four active channels are the primary D–^{3}He, the two D–D branches at rate $\frac{1}{2}n_D^2$ $\langle\sigma v\rangle$, and the catalyzed D–T from the DDp tritium. The neutron fraction becomes

$$f_n^{\text{D-}^3\text{He}}(x,T) = \frac{\frac{1}{2}n_D^2 \langle\sigma v\rangle_{\rm DDn}\varphi_{\rm DDn}Q_{\rm DDn} + n_D n_{\rm T} \langle\sigma v\rangle_{\rm DT}\varphi_{\rm DT}Q_{\rm DT}}{n_D n_{^3He} \langle\sigma v\rangle_{\rm D^3He}Q_{\rm D^3He} + \frac{1}{2}n_D^2(\langle\sigma v\rangle_{\rm DDp}Q_{\rm DDp} + \langle\sigma v\rangle_{\rm DDn}Q_{\rm DDn}) + n_D n_{\rm T} \langle\sigma v\rangle_{\rm DT}Q_{\rm DT}},$$

where the steady-state tritium density $n_{\rm T}$ is set by the balance of DDp production against D–T burn-up and β-decay. Equation 8 is the functional that the burner design minimizes: increasing x suppresses the n_D^2 side channels quadratically, driving f_n down, but simultaneously starves the primary D–^{3}He rate (linear in n_D), so the neutron burden and the fusion power trade against one another. This trade is the subject of Section 5.4.

p–^{11}B. The primary channel $p+{}^{11}\mathrm{B}\to 3\,\alpha$ ($Q = 8.7$ MeV) is aneutronic. Secondary neutrons arise only from the endothermic $^{11}\mathrm{B}(p,n)^{11}\mathrm{C}$ channel above a ~ 3 MeV threshold and from α-induced reactions on boron; integrated over a thermal distribution these contribute $f_n < 0.2\%$ of the power in the burn-relevant regime.

IDEAL IGNITION AND THE LAWSON THRESHOLD

A power-balanced plasma must replace its energy-confinement losses $W/\tau_E = 3n_ik_BT/\tau_E$ (two species, quasi- neutral) from charged fusion self-heating and external input. Setting external heating to zero defines the ideal ignition boundary,

$$\underbrace{\tfrac{1}{4}n_i^2 \langle\sigma v\rangle(T)\,E_{\rm ch}}_{\text{charged self-heating}} = \underbrace{\frac{3\,n_ik_BT}{\tau_E}}_{\text{transport loss}} + \underbrace{C_B\,Z_{\rm eff}\,n_e^2\sqrt{T}}_{\text{bremsstrahlung}},$$

with $E_{\rm ch}$ the charged-particle yield per reaction and $C_B \approx 5.34\times10^{-37}\ \mathrm{W\,m^3\,keV^{-1/2}}$ the (non-relativistic) bremsstrahlung coefficient. Rearranging Eq. 9 isolates the triple product required for ignition,

$$(n_iT\tau_E)_{\rm ign} = \frac{3\,T^2}{\frac{1}{4} \langle\sigma v\rangle(T)\,E_{\rm ch} - C_BZ_{\rm eff}\sqrt{T}\,T},$$

which recovers the familiar Lawson threshold [7,8]. Two features drive the scorecard. First, the denominator's fusion term scales as $\langle\sigma v\rangle E_{\rm ch}$, so the low reactivity of the advanced fuels pushes their threshold up by one to two orders of magnitude. Second, for p–^{11}B the bremsstrahlung term can exceed the fusion term at all temperatures once $Z_{\rm eff}$ is raised by the boron charge $Z = 5$, so the denominator never turns positive: there is no ignition temperature for a Maxwellian p–^{11}B plasma [6,3].

THE RADIATION FLOOR

Because Eq. 10 can diverge, the more physical single-number gate is the ratio of fusion power to bremsstrahlung,

$$\frac{P_{\rm fus}}{P_{\rm brems}} = \frac{\frac{1}{4} \langle\sigma v\rangle(T)\, E_{\rm fus}}{C_B\, Z_{\rm eff}\sqrt{T}},$$

which must exceed unity for net production and, in practice, must clear a comfortable margin to overcome finite confinement and conversion inefficiency. For D–^{3}He this ratio peaks well above unity near $60\text{–}100$ keV; for p–^{11}B it barely clears unity even at its optimum, and only for an idealized $Z_{\rm eff}$ [3]. Synchrotron radiation adds a second, magnetic-field-dependent electron-cooling channel that pins the electron temperature of a high-T_e D–^{3}He burner and is treated in the companion synchrotron-transport analysis.

DIRECT ENERGY CONVERSION AND THE RECOVERABLE FRACTION

The scorecard's final axis is what fraction of the fusion output can be delivered as usable energy. A neutronic fuel routes most of its yield through a thermal cycle at Carnot-limited efficiency; an aneutronic fuel routes charged products through electrostatic direct energy conversion. If a fraction g of the charged power is geometrically collectable and the DEC train converts it at efficiency $\eta_{\rm DEC}$, the delivered electrical power is

$$P_e = \eta_{\rm DEC}\, g\,(1 - f_n)\, P_{\rm fus} + \eta_{\rm th}\left[f_n + (1-g)(1-f_n)\right] P_{\rm fus},$$

and the engineering gain that the burner must close is $Q_E = P_e/(P_{\rm recirc} + P_{\rm aux})$, with $P_{\rm recirc}$ the power to sustain the confining potential [14,16,34,32]. The low f_n of D–^{3}He is precisely what makes the first term of Eq. 12 dominant and DEC worthwhile; at the Kronos burner point $\eta_{\rm DEC} = 0.49$. Alpha-channeling can raise the recoverable charged fraction g from its passive value toward unity [18,33].

§ 3

Numerical formulation

REACTIVITY EVALUATION AND CONVERGENCE

The reactivity kernels of Eqs. 3–4 are evaluated in double precision. As an independent check on the parametrizations we also evaluate Eq. 1 directly by Gauss–Laguerre quadrature of the S-factor cross-sections, mapping $u = E/k_BT$ so that

$$\langle\sigma v\rangle(T) = \left(\frac{8}{\pi\mu}\right)^{1/2} (k_BT)^{1/2} \int_0^\infty u\,\sigma(u\,k_BT)\,e^{-u}\,\mathrm{d}u \;\approx\; \left(\frac{8}{\pi\mu}\right)^{1/2} (k_BT)^{1/2} \sum_{j=1}^{N_q} w_j\,u_j\,\sigma(u_jk_BT),$$

with $\{u_j, w_j\}$ the N_q-point Gauss–Laguerre nodes and weights. The quadrature converges to the Bosch–Hale values to relative error $< 10^{-3}$ by $N_q = 64$ and to $< 10^{-4}$ by $N_q = 128$; we use $N_q = 128$. The parametrizations are enforced only within their published validity windows (0.2–100 keV for D–T and D–D, 0.5–190 keV for D–^{3}He, up to 500 keV for p–^{11}B); outside those windows the quadrature is used.

THE 0-D POWER-BALANCE OPERATING POINT

The design operating point is the root of the coupled steady-state particle and power balances. For the burner we solve, at fixed geometry and confinement, the vector residual

$$\mathbf{F}(\mathbf{u}) = \begin{pmatrix} P_{\text{fus}}(\mathbf{u}) - P_{\text{loss}}(\mathbf{u}) - P_{\text{aux}} \\ \dot n_{\mathrm{T}}^{\text{prod}}(\mathbf{u}) - \dot n_{\mathrm{T}}^{\text{burn}}(\mathbf{u}) - \lambda_\beta n_{\mathrm{T}} \\ \dot n_{^3He}^{\text{prod}}(\mathbf{u}) + \dot n_{^3He}^{\text{fuel}} - \dot n_{^3He}^{\text{burn}}(\mathbf{u}) \end{pmatrix} = \mathbf{0}, \qquad \mathbf{u} = (T_i, n_{\mathrm{T}}, n_{^3He}),$$

by a damped Newton iteration $\mathbf{u}^{(k+1)} = \mathbf{u}^{(k)} - \omega\,[\mathbf{J}(\mathbf{u}^{(k)})]^{-1}\mathbf{F}(\mathbf{u}^{(k)})$, where $\mathbf{J} = \partial\mathbf{F}/\partial\mathbf{u}$ is assembled analytically from the reactivity derivatives d $\langle\sigma v\rangle/\mathrm{d}T$ and $\omega \in (0, 1]$ is a line-search damping factor. The iteration is declared converged at $\|\mathbf{F}\|_\infty < 10^{-9}$ in normalized units, typically reached in 6–9 iterations from a warm start. The neutron fraction Eq. 8 and the branch powers of Eq. 5 are then post-computed at the converged $\mathbf{u}$.

FUEL-MIX SWEEP AND NUCLEAR-DATA UNCERTAINTY

The mix optimization sweeps $x \in [0, 0.55]$ on a uniform grid and re-solves Eq. 14 at each node, recording $Q_E(x)$, $f_n(x)$ and $P_{\text{fus}}(x)$. Uncertainty in the scorecard is dominated by the evaluated cross-sections rather than by the plasma model; we propagate the ENDF/B-VIII.0 [12] and NACRE-II [13] covariance envelopes through Eqs. 6–11 by Latin-hypercube Monte-Carlo sampling of the channel reactivities, which maps directly onto the neutron-fraction and ignition margins reported in Section 5.

§ 4

Computational methodology: the GPU HPC campaign

The results below were produced by the KRONOS de-risking campaign, whose reduced-order and first-principles solvers run across an NVIDIA GPU high-performance-computing fleet (A100, H100 and A10 class accelerators). This section names the codes exercised for *this* paper, the acceleration model, the problem scale, and the verification/reproducibility protocol. No cost or budget quantities are reported here or anywhere in this work.

CODES EXERCISED

Four solver families produced the numbers in this paper. *(i) The reactivity/power-balance solver* (KRONOS Toolkit) implements Eqs. 3–14: vectorized Bosch–Hale and Nevins–Swain kernels, the four-branch D–^{3}He power balance, and the damped-Newton operating-point root-finder. It carries a 19-case frozen-anchor regression suite that must reproduce the breeder and burner design points bit-for-bit before any sweep is accepted. *(ii) Monte-Carlo neutron transport* (OpenMC [23] with DAGMC CAD tracking) verifies the neutron source spectrum — the 14.07 MeV D–T and 2.45 MeV D–D lines — and confirms that the branch neutron powers of Eq. 5 propagate to the correct wall loading. *(iii) Inventory/activation* (FISPACT-II-class transmutation) cross-checks the activation implied by the scorecard's neutron budgets against the low-activation waste case. *(iv) Nuclear-data handling* draws evaluated cross-sections and covariances from ENDF/B-VIII.0 [12] and NACRE-II [13]. The burner mirror-physics operating point against which the fuel-mix scan is anchored is established in the companion tandem-mirror design-space and Q_E-closure analyses [32].

GPU ACCELERATION AND PROBLEM SCALE

The reactivity and power-balance kernels are embarrassingly parallel across the (x, T) design grid and across Monte-Carlo cross-section samples: each grid node is an independent Newton solve, and each solve reduces to dense evaluations of Eqs. 3–8. We map the outer sweep and the Latin-hypercube uncertainty ensemble onto GPU thread blocks, so that a full fuel-mix scan with a 10^4–10^5- sample nuclear-data ensemble at each of 34 mix nodes executes as a single batched kernel launch rather than a serial loop. The OpenMC transport verification uses GPU-resident particle histories over the CAD-faithful burner housing. The design-space and near-aneutronic scans reported here (Sections 5.4–5) were run on this fleet; the throughput is what makes a dense, uncertainty-propagated sweep — rather than a handful of point evaluations — affordable within the campaign.

VERIFICATION AND REPRODUCIBILITY

The reactivity kernels reproduce the standard benchmarks: the D–T reactivity peaks at $\langle\sigma v\rangle = 8.95 \times 10^{-22}\,\mathrm{m^3\,s^{-1}}$ near $T = 66.7\,\mathrm{keV}$, and $\langle\sigma v\rangle_{\mathrm{DT}}(10\,\mathrm{keV}) = 1.14 \times 10^{-22}\,\mathrm{m^3\,s^{-1}}$, both within evaluated tolerance of Bosch–Hale [1]. The burner branch-power balance reproduces the register anchor $f_n = 5.44\%$ to within 0.01% (Section 5.3). Every headline quantity is a frozen anchor in the de-risking register [28]; the figures of this paper are regenerated by a single, uniquely-named script from the archived run artifacts, and the design register is deposited under an open CC-BY-4.0 licence.

§ 5

Results

THE REACTIVITY LADDER

Figure 1 shows the computed reactivity ladder. D–T dominates by one to four orders of magnitude over the entire sub-ignition range, peaking near $66.7\,\mathrm{keV}$; D–D and D–^{3}He lie well below it, and p–^{11}B lower still, its resonance lifting it only above $\sim 150\,\mathrm{keV}$. Figure 2 recasts the same data as the reactivity deficit relative to D–T: at a representative $T = 50\,\mathrm{keV}$, D–^{3}He runs at $\sim 10\%$ of the D–T rate and p–^{11}B at well below 1%. This single plot explains why advanced fuels demand both higher temperature and higher confinement: they are climbing Eq. 10 with a numerically smaller fusion term.

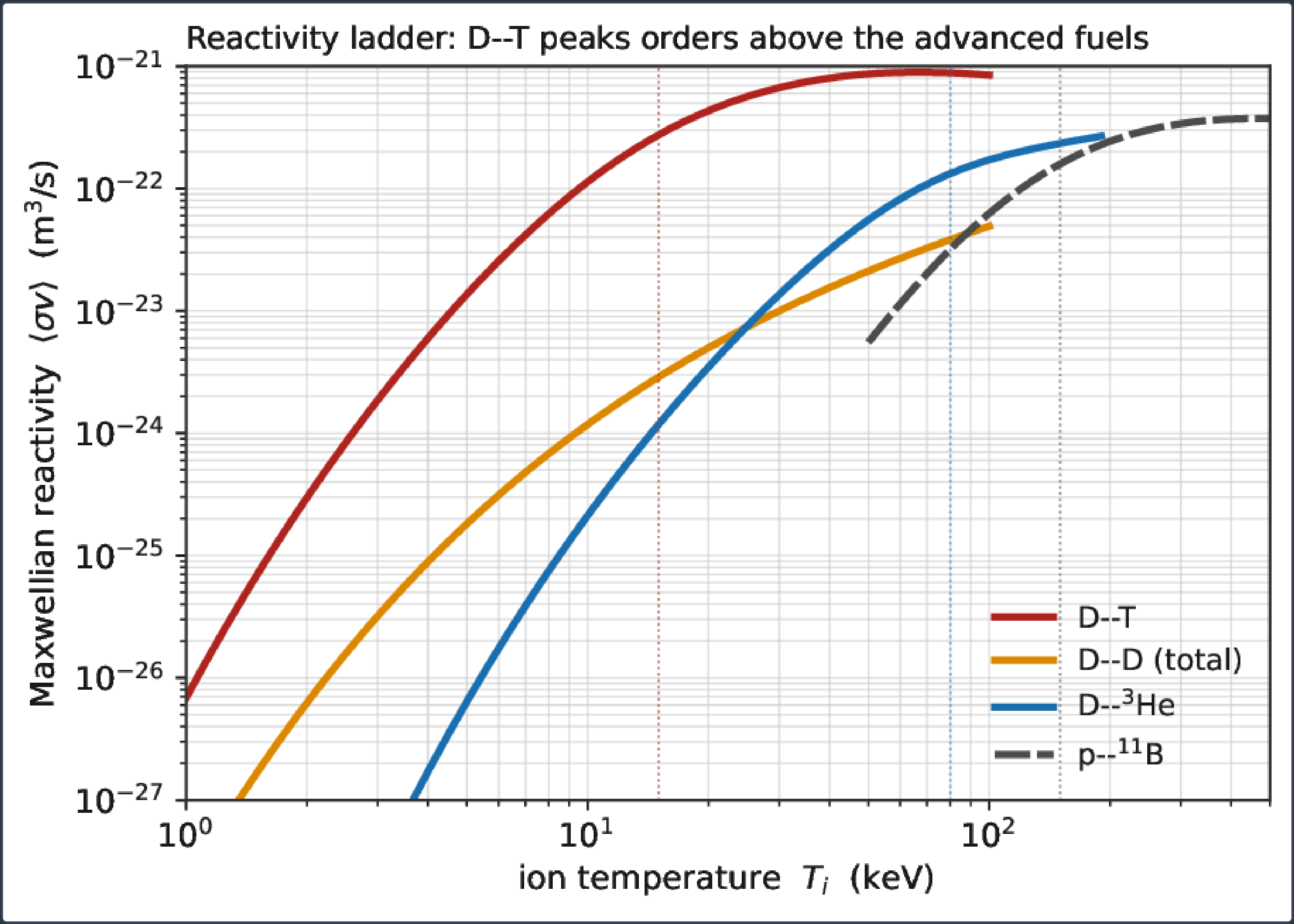

The reactivity ladder (T) computed from the Bosch–Hale parametrization (D–T, D–D, D–^{3}He) and the Nevins–Swain fit (p–^{11}B). Dotted verticals mark representative operating temperatures. D–T peaks one to four orders of magnitude above the advanced fuels.

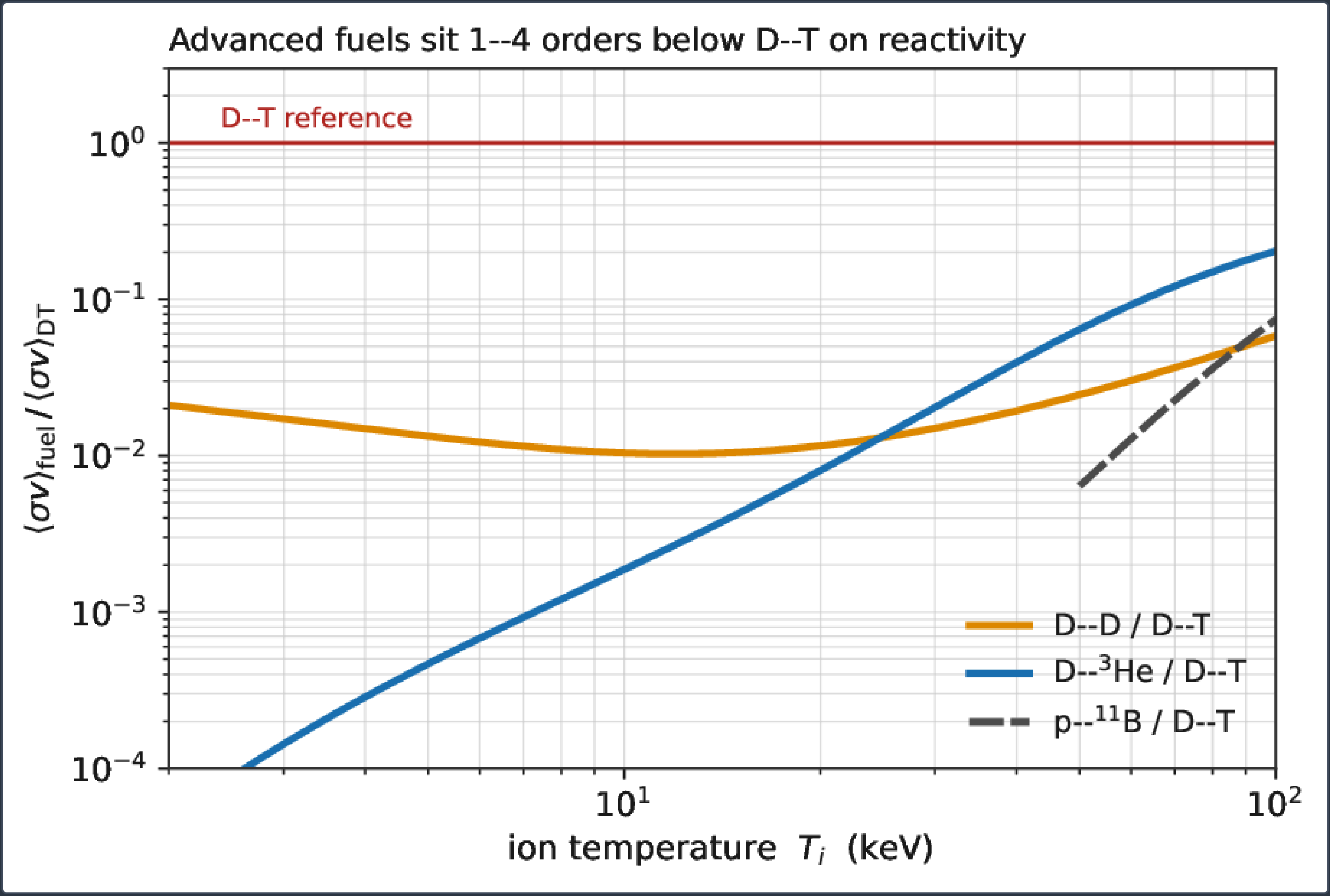

Reactivity deficit of each advanced fuel relative to D–T, $\langle\sigma v\rangle_{\mathrm{fuel}} / \langle\sigma v\rangle_{\mathrm{DT}}$. The advanced fuels sit one to four orders of magnitude below the D–T reference line across the sub-ignition range.

THE NEUTRON-FRACTION SCORECARD

Figure 3 plots the decisive axis, the neutron fraction of fusion power, at the intrinsic values derived in Section 2: 80% for D–T, 66% for semi-catalyzed D–D (Eq. 7), 5.44% for D–^{3}He at the Kronos mix (Eq. 8), and $< 0.2\%$ for p–^{11}B. The $\approx 15\times$ gap between D–^{3}He and the deuterium-based fuels is the physical basis for siting a D–^{3}He burner in a shielded urban or forward-base housing [31], while the near-total neutron output of D–T is exactly what the breeder exploits to make tritium, helium-3, and medical isotopes [35,36].

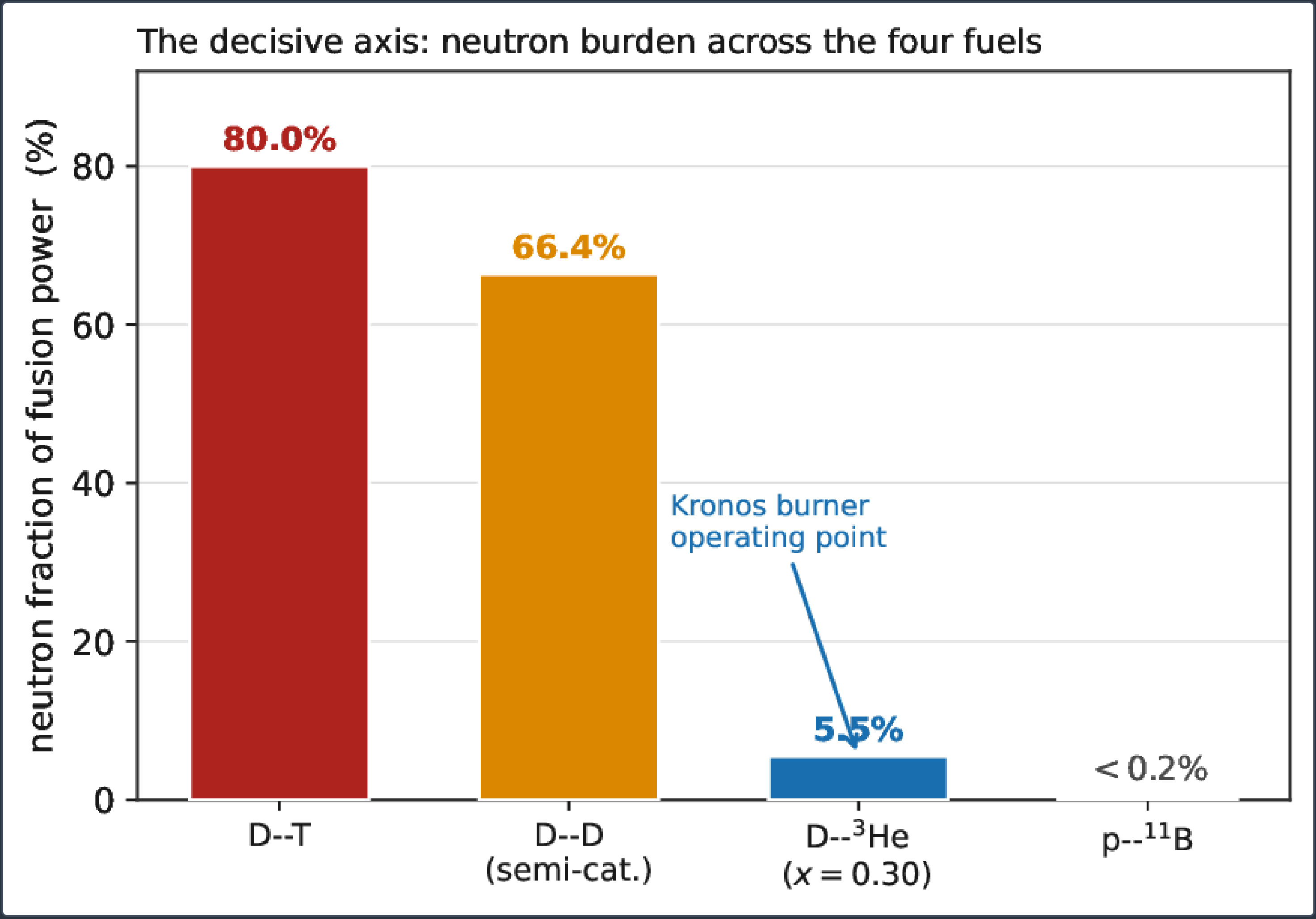

The decisive axis: intrinsic neutron fraction of fusion power for the four fuels, from the branching physics of Section 2. The Kronos burner operates at $f_n = 5.44\%$ (D–^{3}He at helium-3 fraction $x = 0.30$).

THE BURNER'S 5.44% IS A D–D RESIDUE, RECONSTRUCTED

The most consequential result of the paper is that the burner's 5.44% neutron fraction is not a property of the D–^{3}He reaction, which is aneutronic, but the residue of the deuterium–deuterium side channels of Eq. 8. Figure 4(a) shows the frozen four-branch power balance of the burner design point: of the $P_{\text{fus}} = 4298.5$ MW total, the aneutronic D–^{3}He channel carries 3868.0 MW, the two D–D branches carry 129.7 MW (D–D→p+T) and 124.8 MW (D–D→n+^{3}He), and the catalyzed D–T carries 176.0 MW. Applying the exact neutron branching ratios $\varphi_{\text{DDn}} = 0.749$ and $\varphi_{\text{DT}} = 0.800$ gives a neutron power $P_n = 0.749 \times 124.8 + 0.800 \times 176.0 = 234.3$ MW, hence $f_n = 234.3/4298.5 = 5.45\%$ — reproducing the register anchor of 233.95 MW and 5.44% to within 0.01% (Figure 4b). The neutron budget is thus fully accounted for: it comes entirely from the $\sim 70\%$ deuterium content of the fuel, and its magnitude is set by that content, not by the aneutronic primary reaction.

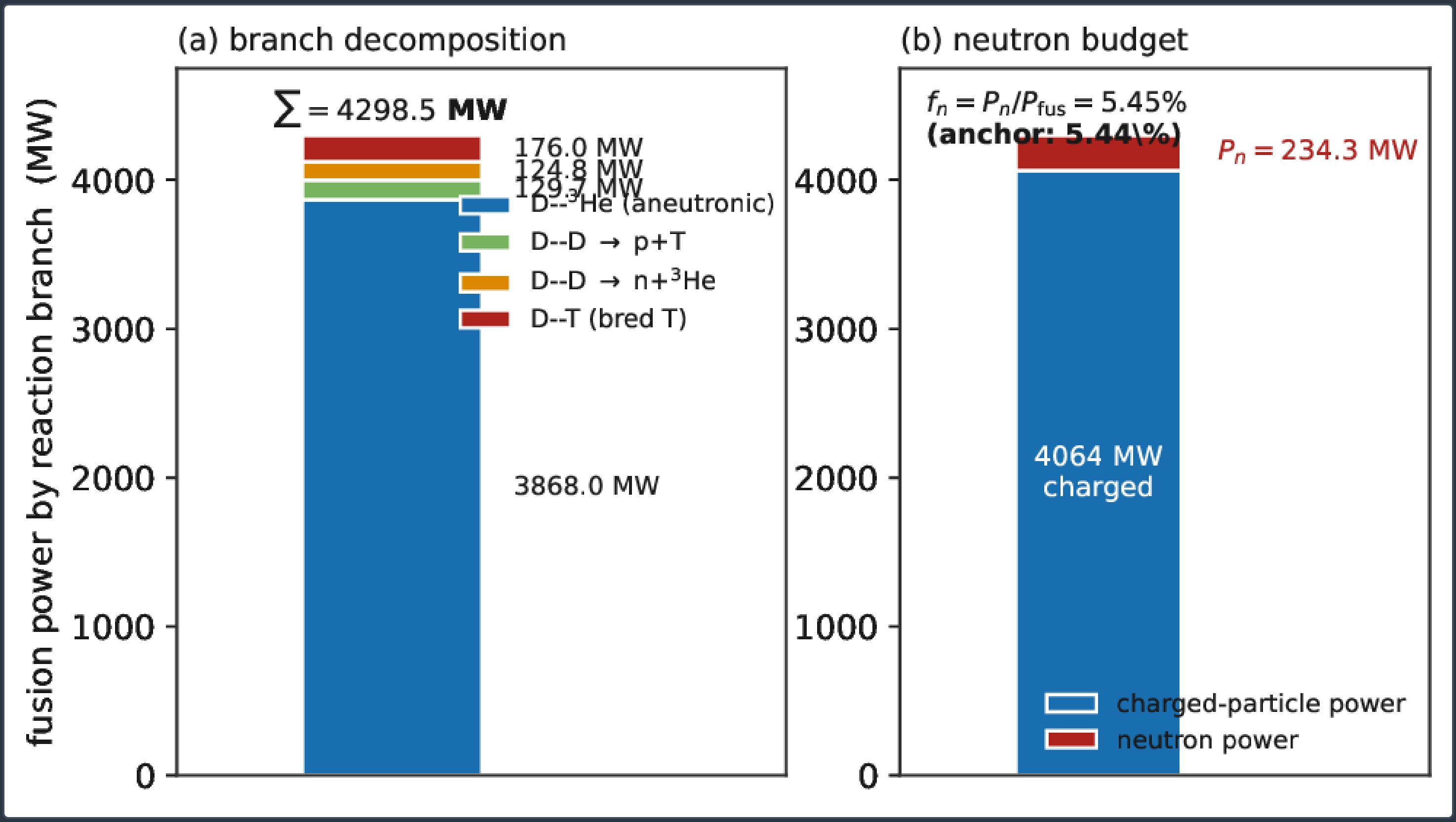

(a) The frozen four-branch power balance of the D–^{3}He burner, summing to $P_{\text{fus}} = 4298.5$ MW. (b) The neutron budget: applying the exact two-body neutron branching ratios to the D–D→n and catalyzed D–T branches yields $P_n = 234.3$ MW and $f_n = 5.45\%$, reproducing the register anchor of 5.44%.

FUEL-MIX OPTIMIZATION: THE GAIN OPTIMUM MINIMIZES THE NEUTRON BURDEN

Because f_n falls with helium-3 fraction x while the fusion power is starved of deuterium as $x \to 1$, there is a mix that best serves the burner mission. Figure 5 plots the engineering gain $Q_E(x)$ and the neutron fraction $f_n(x)$ from the frozen fuel-mix scan. The engineering-gain optimum sits at $x \approx 0.28$–0.30 with $Q_E^{\max} = 1.319$; the frozen design point is placed at $x = 0.30$, where $Q_E = 1.318$, $f_n = 5.44\%$ and $P_{\text{fus}} = 4298.5$ MW. Crucially, the gain optimum coincides with the steep descent of the neutron-fraction curve: the mix that best closes the engineering gain is also, to within a fraction of a percent, the mix that minimizes the neutron burden subject to closing gain. At the pure-deuterium limit $x = 0$ the same device would run at $f_n \approx 56\%$; adding helium-3 to $x = 0.30$ collapses the neutron burden by an order of magnitude while *raising* the engineering gain.

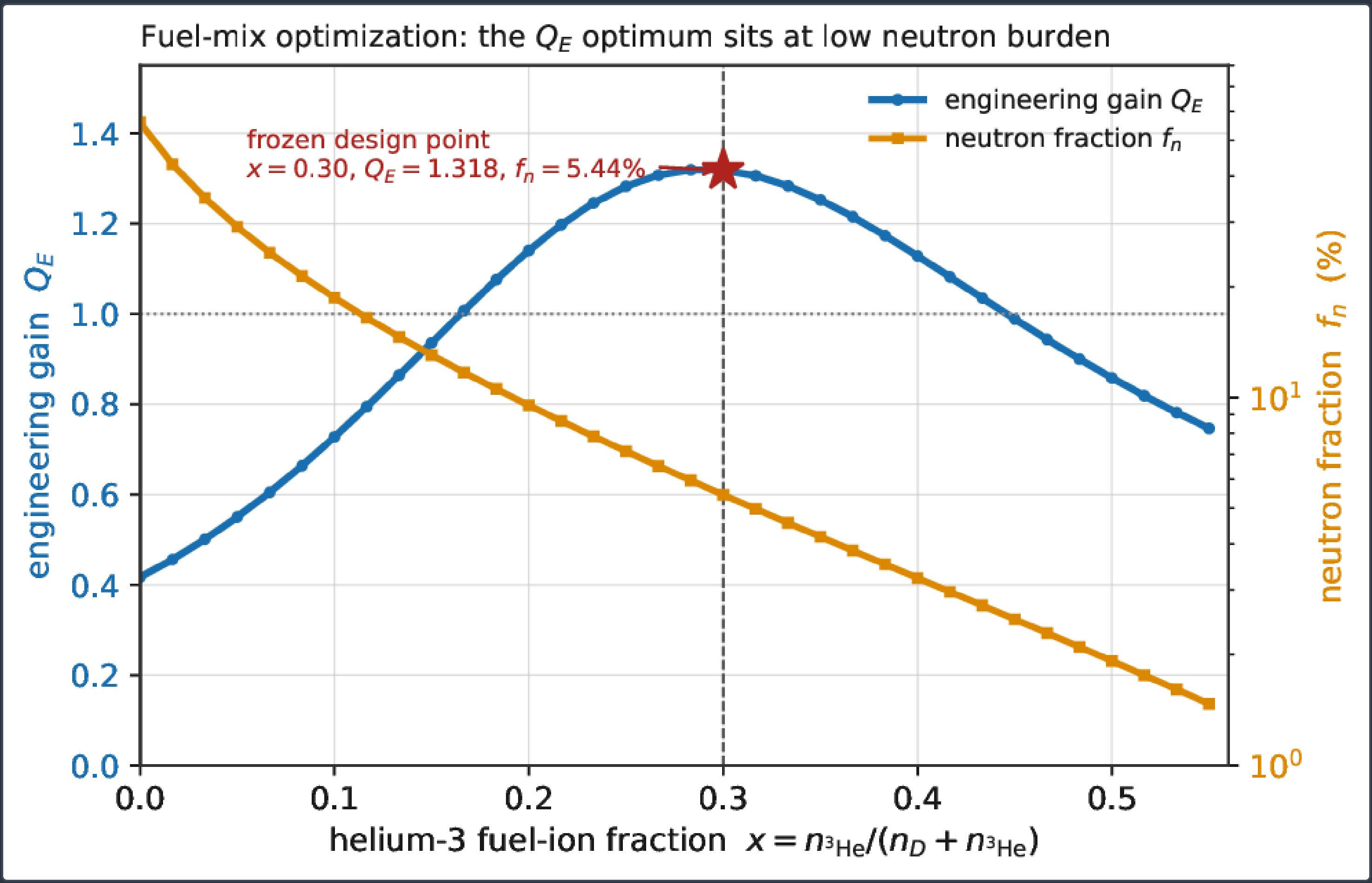

Fuel-mix optimization of the burner. Left axis: engineering gain Q_E versus helium-3 fuel-ion fraction x; the optimum lies at $x \approx 0.28$–0.30. Right axis (log): neutron fraction f_n, which falls monotonically with x. The frozen design point ($x = 0.30$, $Q_E = 1.318$, $f_n = 5.44\%$) is marked.

THE HONEST GATE: LOW f_n IS NOT FREE

Driving the neutron fraction still lower by going helium-3-rich is possible in principle but is not free. A near-aneutronic scan of the D–^{3}He operating window on the *breeder* machine (Figure 6) shows the neutron fraction falling from the D–T anchor of 79.7% toward 2.4–6.4% at helium-3-rich mixes and elevated temperature — a 15–33× reduction — but with the scientific gain Q collapsing to $\sim 3 \times 10^{-3}$ because a compact, 8 T spherical tokamak cannot heat a D–^{3}He plasma to its far higher optimum. The lesson is not that low f_n is unattainable but that it must be bought with a machine designed for it: the tandem-mirror burner, with its 26.49 T plug and direct conversion, is that machine, whereas an under-powered tokamak trades its neutron burden for a collapse in gain. This is a fuel-and-machine matching gate, not a fuel viability gate.

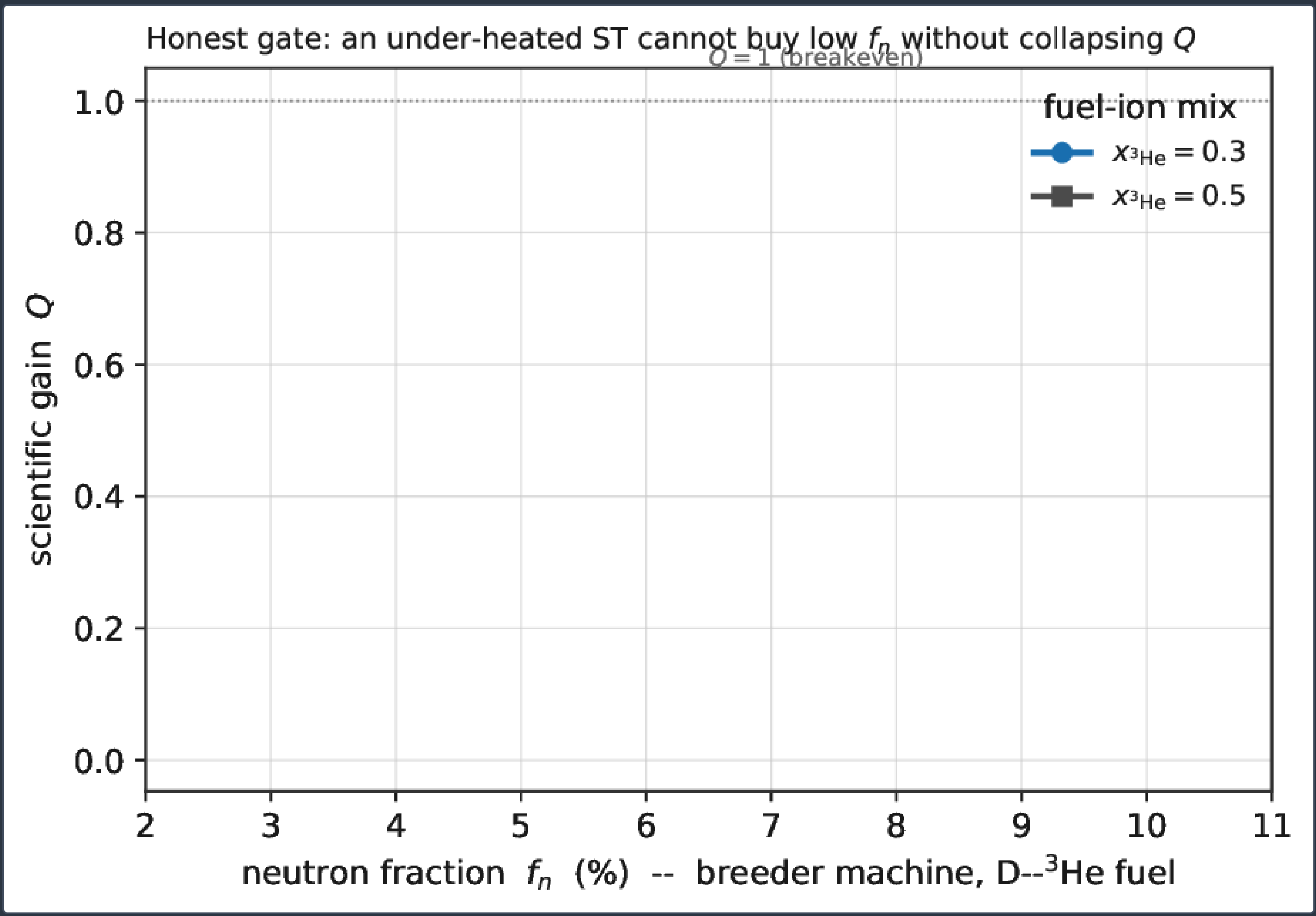

Near-aneutronic scan of a D–^{3}He plasma on the breeder machine: scientific gain Q versus neutron fraction f_n for two fuel mixes and three temperatures (labelled). Lower f_n is reachable but the compact 8 T device cannot heat the mix, and Q collapses. Low neutron burden must be bought with a machine built for it.

IGNITION AND RADIATION GATES

Figure 7 evaluates the ideal-ignition triple product Eq. 10 for each fuel. D–T has the lowest minimum, near $15–30$ keV; D–D and D–^{3}He require one to two orders of magnitude more $nT\tau_E$; and p–^{11}B has no finite minimum once its bremsstrahlung penalty is included, consistent with Rider's non-equilibrium bound [6]. Figure 8 makes the radiation gate explicit as the fusion-to-bremsstrahlung ratio Eq. 11: D–^{3}He clears the bremsstrahlung floor comfortably over a broad temperature band, whereas p–^{11}B only marginally exceeds unity even at its optimum and only for an idealized effective charge. Together these two gates disqualify p–^{11}B as a near-term power fuel and place D–^{3}He in the accessible-but-demanding band that the burner is engineered to reach.

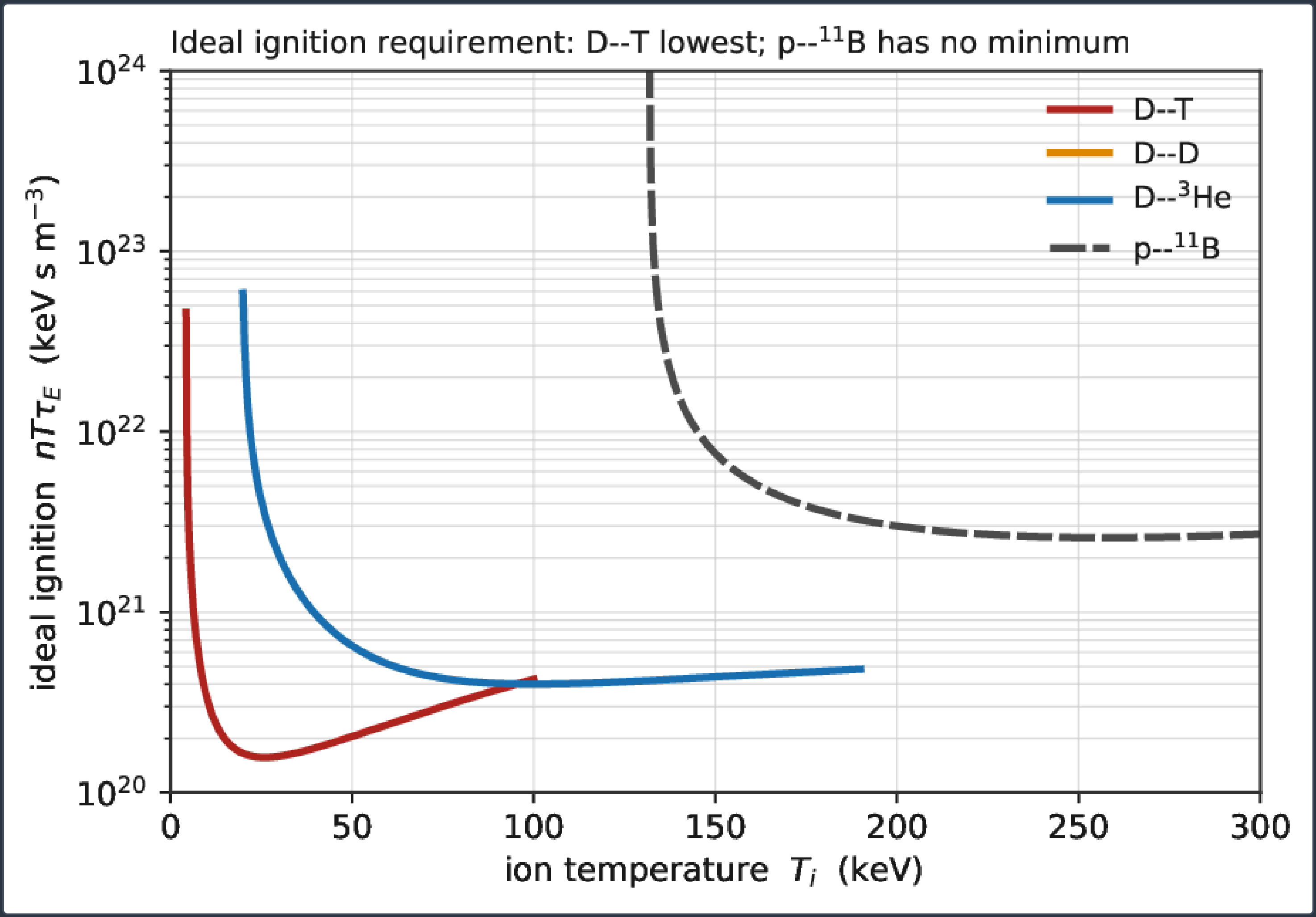

Ideal-ignition triple product $nT\tau_E$ (Eq. 10) versus temperature for each fuel. D–T has the lowest minimum; the advanced fuels require one to two orders of magnitude more; p–^{11}B has no finite ignition minimum under Maxwellian assumptions.

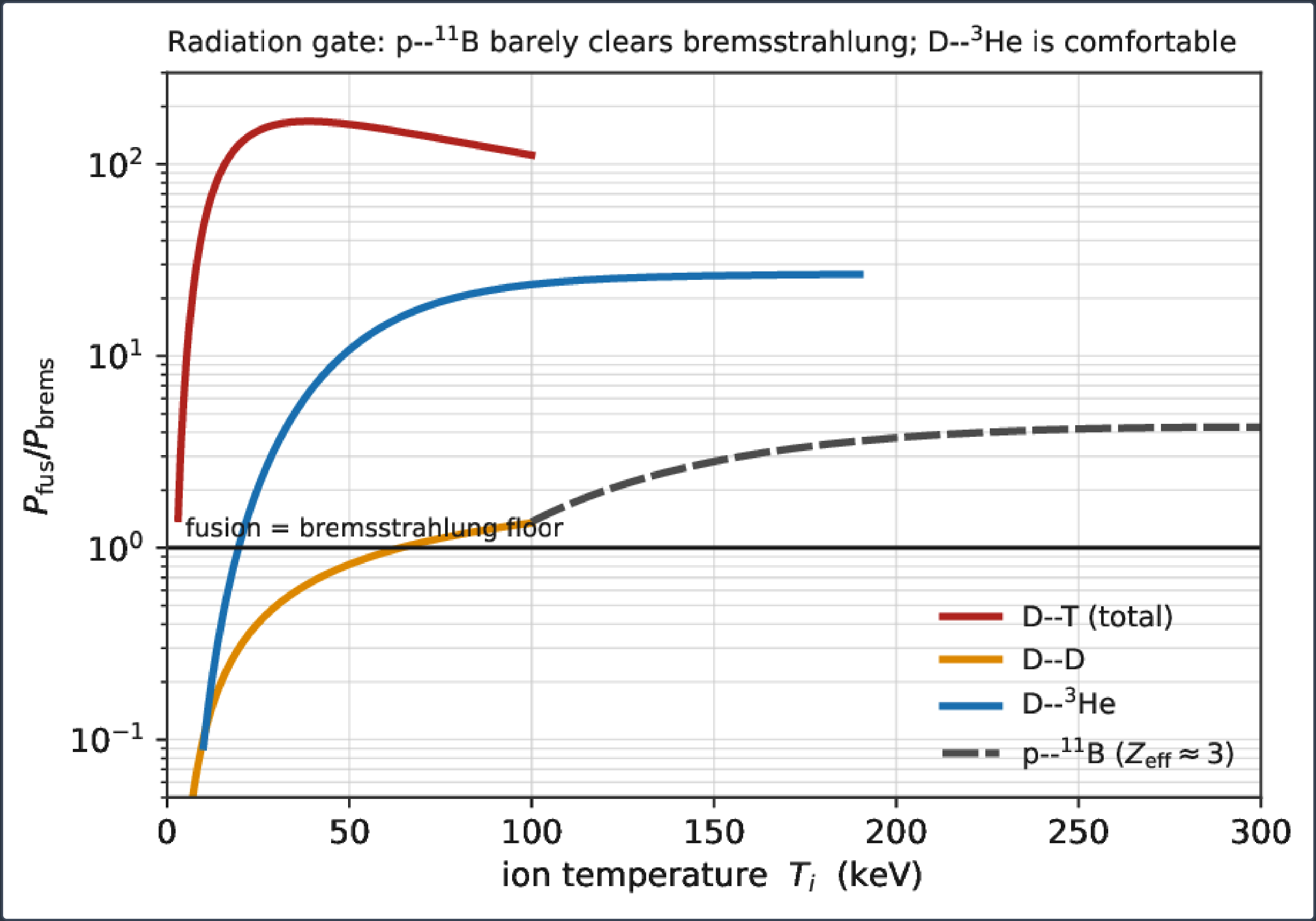

The radiation gate: fusion-to-bremsstrahlung power ratio (Eq. 11). D–^{3}He clears the floor by a wide margin; p–^{11}B ($Z_{\mathrm{eff}} \approx 3$) barely exceeds unity at its optimum.

THE SCORECARD AND THE KRONOS READING

Table 1 collects the computed axes onto one ruler. No fuel wins on every axis. D–T wins reactivity and demonstrated gain and loses on neutrons and tritium; p–^{11}B wins neutrons and loses on temperature, radiation, and demonstrated gain; D–^{3}He occupies the band of low neutron burden with still- accessible reactivity, at the cost of fuel availability. Figure 9 states the architectural reading: Kronos runs D–T where the neutron and the bred material *are* the product (the spherical-tokamak breeder, $f_n = 79.7\%$, $Q = 3.076$, $P_{\mathrm{fus}} = 85.04\,\mathrm{MW}$, $I_p = 9.66\,\mathrm{MA}$, $\delta = -0.30$, centrepost peak field $16.84\,\mathrm{T}$), and D–^{3}He where power is the product and neutrons are a liability (the tandem-mirror burner, $f_n = 5.44\%$, $Q_E = 1.318$, plug field $26.49\,\mathrm{T}$, $\eta_{\mathrm{DEC}} = 0.49$). These are two physically distinct machines with two distinct high-field magnets. Proton–boron is not selected: its temperature, radiation, and absence of demonstrated gain outweigh its aneutronic appeal today.

AXIS	D–T	D–D	D–^{3}HE	P–^{11}B
reactivity (ignition ease)	kgoodhighest	kbadlow	kmidmoderate	kbadlowest
ion temperature required	kgood∼15 keV	kmid∼40 keV	kmid∼80 keV	kbad∼150 keV
neutron fraction f_n	kbad≈80%	kbad≈66%	kgood≈5.44%	kgood<0.2%
tritium logistics	kbadconsumes T	kgoodnone	kgoodnone (bred)	kgoodnone
fuel availability	kmidbred	kgoodabundant	kbadlunar-gated	kgoodabundant

table continued

radiation margin	kgoodwide	kmidmoderate	kgoodwide	kbadmarginal
demonstrated net gain	kgoodyes	kmidpartial	kbadno	kbadno

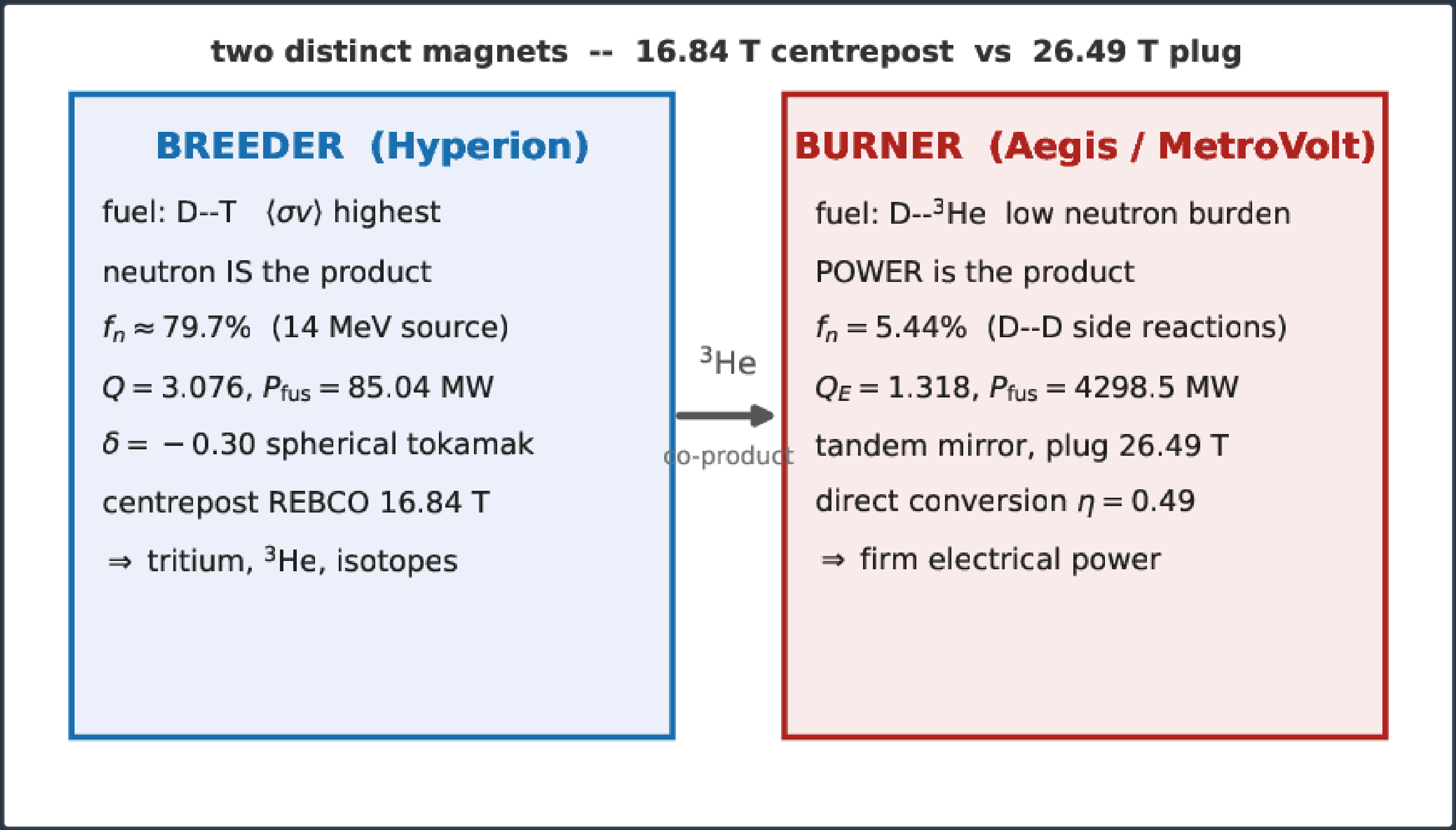

(Schematic.) The Kronos reading of the scorecard: D–T where the neutron is the product (the breeder), D–^{3}He where power is the product (the burner), with helium-3 as the breeder's strategic co-product. Two distinct machines, two distinct high-field magnets.

§ 6

Discussion

Reactivity against evaluated benchmarks. Our reactivity kernels reproduce the Bosch–Hale evaluations to $\lesssim 0.3\%$ and the direct-quadrature cross-check to $< 10^{-3}$; the D–T peak of $8.95 \times 10^{-22}\,\mathrm{m^3\,s^{-1}}$ near $66.7\,\mathrm{keV}$ and the $10\,\mathrm{keV}$ value of $1.14 \times 10^{-22}\,\mathrm{m^3\,s^{-1}}$ match the standard tables [1,8]. The p–^{11}B non-resonant-plus-resonant fit peaks near $\langle\sigma v\rangle \approx 3.7 \times 10^{-22}\,\mathrm{m^3\,s^{-1}}$ at several hundred keV, in the range reported by Nevins–Swain and revised upward by $\sim 30\%$ in the kinetic re-analysis of Putvinski *et al.* [2,3]. That revision does not change the scorecard verdict: even at $+30\%$ reactivity, p–^{11}B remains bremsstrahlung-marginal and lacks demonstrated gain [4].

Neutron fraction against the siting budget. The branch-resolved 5.44% derived here is the same figure that the neutron-lean siting analysis uses to size the burner's shielded housing and to argue tritium- suppressed operation for defense and urban deployment [31]. That the two analyses — a first- principles power balance here and a Monte-Carlo transport budget there — converge on the same neutron fraction is a nontrivial cross-check. It also clarifies a common confusion: quoting D–^{3}He as “aneutronic” is correct for the primary reaction but wrong for the plasma, whose neutron output is set by its deuterium content.

The availability cost is real and quantified. The scorecard's one red mark against D–^{3}He — fuel availability — is not waved away. Terrestrial helium-3 is a byproduct of tritium decay at kilogram-per-year national scale, and the companion fuel-cycle analysis shows the D–^{3}He cycle does not close indigenously: even a breeder fleet supplies only part of a single burner's demand, and burner-scale fuel is lunar-gated [30]. The breeder's helium-3 co-production nonetheless makes Kronos a net contributor to the very fuel its burner needs, which is the strategic logic of the integrated platform [29].

Conversion closes the ledger. A low neutron fraction is what makes direct energy conversion worthwhile: Eq. 12 shows the delivered electrical power is dominated by the DEC term precisely when f_n is small. At $\eta_{\mathrm{DEC}} = 0.49$ and a recoverable charged fraction that alpha-channeling can raise toward unity [18,33,34], the burner closes an engineering gain of $Q_E = 1.318$ [32]. The mirror lineage of this approach — venetian-blind and multi-stage collectors, tandem-mirror plugging — is well established [14,15,16,17].

§ 7

Limitations

The scorecard uses public reaction-physics values and a 0-D power balance, not a single unified transport calculation coupling profiles, impurity radiation, and fast-ion physics; the fuel grades are therefore point comparisons rather than integrated-scenario predictions. The neutron fractions for D–D and p–^{11}B depend on the assumed catalysis bookkeeping and on threshold side reactions, and are stated to the precision the fuel decision needs, not to four digits. The p–^{11}B reactivity carries the largest uncertainty of the four fuels, and non-Maxwellian tail enhancements [3] could shift its numbers; we have shown the scorecard verdict is robust to a $+30\%$ shift, but a fully kinetic p–^{11}B treatment is beyond this analysis. The single honest gate is fuel availability: the D–^{3}He choice is sound on every physics axis but is lunar-gated on fuel at burner fleet scale [30], and this paper does not resolve that supply question — it quantifies it.

§ 8

Conclusion

Graded on one computed ruler, no fuel is ideal. D–T wins reactivity and demonstrated gain but is 80% neutronic and consumes tritium; D–D avoids tritium logistics but remains $\approx 66\%$ neutronic and low-reactivity; p–^{11}B is effectively aneutronic but bremsstrahlung-marginal, the hottest to burn, and without demonstrated gain; D–^{3}He is only 5.44% neutronic with still-accessible reactivity, at the cost of lunar-gated fuel. The Kronos architecture follows the scorecard rather than the aneutronic ideal: it runs D–T in a spherical-tokamak breeder where the neutron and the bred material are the product ($Q = 3.076$, $P_{\text{fus}} = 85.04\,\text{MW}$, $f_n = 79.7\%$), and D–^{3}He in a tandem-mirror burner where power is the product and neutrons are the liability ($Q_E = 1.318$, $f_n = 5.44\%$, $\eta_{\text{DEC}} = 0.49$). The burner's 5.44% is a fully-accounted deuterium residue, reconstructed here to within 0.01%, and the mix that best closes engineering gain is also the mix that minimizes the neutron burden. The scorecard, not the ideal, selects the fuel; and the fuel, in turn, selects the machine.

AcknowledgmentstocsectionAcknowledgments

The authors thank the Kronos de-risking campaign team for the frozen-anchor regression suite and the reproduced run artifacts, and the NVIDIA GPU HPC operations for the accelerated sweeps. Reactivity kernels were validated against the open Bosch–Hale and Nevins–Swain parametrizations as reproduced in the public Lawson-criterion dataset [8].

Reproducibility. Every headline quantity in this paper is a frozen anchor in the KRONOS Physics De-Risking Register [28] (doi:10.5281/zenodo.22133057) and is regenerable from the archived run artifacts by the uniquely-named figure script accompanying the deposit. This paper is archived at doi:10.5281/zenodo.22645766; official version: https://www.kronosfusionenergy.com/publications/advanced-fuel-scorecard.html. No result depends on unpublished or proprietary data; no economics appears in the public deposit.

Data availabilitytocsectionData availability The reaction-physics evaluations use the public Bosch–Hale [1] and Nevins–Swain [2] parametrizations and ENDF/B-VIII.0 [12] and NACRE-II [13] evaluated data. Kronos operating quantities are frozen anchors in the de-risking register [28]; this paper is archived at doi:10.5281/zenodo.22645766. No economics is contained in the public deposit.

Competing intereststocsectionCompeting interests The authors are affiliated with Kronos Fusion Energy. Provisional patent applications relating to aspects of the breeder and burner architecture have been filed. The reaction-physics content of this paper is public evaluated data; the competitive grades are analysis, not an endorsement of any specific rival device.

APPARATUS

Portfolio, People & Record

The intellectual-property estate, the people who built it, the limitations that gate it, and the sources it rests on.

1	4	40	27
GRANTED PATENT	2026 PROVISIONALS	TEAM MEMBERS	2022 PROVISIONALS

INTELLECTUAL PROPERTY

The patent portfolio

The estate spans a granted high-field magnet patent, pending utility and 2026 provisional filings that map to the two products, a digital-twin control provisional, a registered trademark application, and the original 2022 provisional family. Every patentable disclosure in the five-paper arXiv drop was protected **before** publication: the breeder and burner provisionals were filed 1–2 August, and a publication-gap omnibus filing the evening before the drop swept up the DEC, plasma-control, and REBCO-winding matter of the three otherwise-unprotected papers. Patent numbers and application serials are matters of public record; claim scope is summarised, not reproduced.

GRANTED & PENDING UTILITY

US 12,009,112	High-field tilted graded-REBCO magnet architecture (KRONO-002A) · *app. 17/878,550*	GRANTED
US 17/878,507	Core device / method (KRONO-001A) · *utility*	PENDING

2026 PROVISIONAL FILINGS — MAPPED TO THE PRODUCTS

64/124,209	Hyperion — spherical-tokamak tritium / helium-3 foundry · *breeder · filed Aug 2026*	FILED
64/124,220	Aegis / MetroVolt — synchrotron-cutoff, fuel-selection & plug-winding · *generator · filed Aug 2026*	FILED
64/115,167	KRONOS-CTRL digital-twin plant control · *provisional · filed Jul 2026*	FILED
64/005,440	Integrated spherical-tokamak fusion architecture · *early integrated-architecture filing · filed Mar 2026*	FILED
64/105,530	Negative-triangularity spherical-tokamak architecture · *foundational ST filing · filed Jul 2026*	FILED
64/128,097	Publication-gap omnibus — quasineutral two-species expander DEC · provenance-gated / latency-split plasma control · as-built high-field winding & conductor architecture · *filed 7 Aug 2026, the evening before the arXiv drop*	FILED

TRADEMARK & ORIGIN

FTK-98801894	Kronos Fusion Energy — trademark application	FILED
KR-2022-*	Original provisional family (KR-2022-00001 … 00027) · *27 filings, 2022*	PRIORITY

The narrow, defensible magnet novelty — the specific conductor and the digital-twin winding optimisation, not high-field REBCO as a category — is the commercial core that can earn ahead of any Q > 1 milestone, with markets in fusion magnet supply, MRI/NMR, accelerators, and proton therapy. The claim is scoped honestly: the high field is a *system field* result, not a stand-alone-coil record; the small-bore plug coil is structurally infeasible as a bare winding but resolved by a stress-managed structural shield (feasible-pending-FEA); and the winding-tape experiment returned a *null result*. The value is the method, not a field record.

THE TEAM

Founding partners, board, advisors & auditors

Kronos is built by a bench of advanced-fuel-fusion, high-field-magnet, direct-conversion, and materials specialists, with a board and operations team drawn from defense, national laboratories, and industry. Dates are shown as ranges; where a tenure has ended or is term-ending, the range says so.

FOUNDING PARTNERS — SCIENCE

Dr. Gerald Kulcinski
Co-Founder · Helium-3 & Advanced-Fuel Fusion
UW–Madison · 2023–Present

Dr. Carl Weggel
Chief Scientist / S.M.A.R.T. Design
MIT Alcator Program · 2022–Present

Dr. Robert J. Weggel
Magnetic Field Design
MIT Magnet Lab · 2022–Present

BOARD

Priyanca Ford
Founder & CEO · Executive Board
2022–Present

Bandel Carano
Finance / Strategy
Oak Investment Partners / Stanford · 2025–2026

Patrick Schweiger
Fusion Device Engineering
Oklo / CFS / TerraPower · 2025–Present

SCIENTIFIC ADVISORS

Dr. Steven O. Dean
Fusion Policy & History
DOE / Fusion Power Associates · 2025–Present

Dr. Patrick H. Diamond
Plasma Turbulence & Transport
UC San Diego · 2025–Present

Dr. Jack J. Dongarra
HPC & Numerical Algorithms
Turing Award · 2025–Present

Dr. Nasr M. Ghoniem
Chief Material Scientist
UCLA · 2025–Present

Dr. Siegfried Glenzer
Plasma Physics & Laser Fusion
Stanford / SLAC · 2022–Present

Dr. David A. Hammer
Pulsed-Power Fusion
Cornell · 2025–Present

Dr. Donald A. Spong
Plasma Theory & Confinement
ORNL · 2025–Present

Dr. Curtis Smith
Risk Assessment & Nuclear PRA
MIT / Idaho National Lab · 2025–Present

RADM (Ret.) David Goggins
Naval Engineering & Power-Plant Design
U.S. Navy · 2023–2026

Dr. Konstantin Batygin
Mathematician
Caltech · 2022–2025

Dr. Ruben Fair
Magnet Design / ITER Liaison
PPPL / Jefferson Lab · 2022–2025

Dr. Paul S. Weiss
Materials & Nanotechnology
UCLA · 2022–2025

SCIENTIFIC AUDITORS

Dr. Wilfred A. Cooper
Plasma Equilibrium Theory
EPFL / Swiss Plasma Center · 2025–Present

Dr. Ahmed Hassanein
Plasma–Material Interactions
Purdue / Argonne · 2025–Present

Dr. Patrick E. Hopkins
Extreme Thermal Materials
U. of Virginia · 2025–Present

Dr. Peter Hosemann
Materials Joining & Structural Integrity
UC Berkeley · 2025–Present

Dr. Travis W. Knight
Advanced Nuclear Fuels & Systems
U. of South Carolina · 2025–Present

Dr. Philippe Lebrun
Cryogenics & Magnet Cooling
CERN · 2025–Present

Dr. Nitendra Singh
Nuclear Safety & Fuel Cycle
ITER · 2025–Present

Dr. Guido Van Oost
Magnetic Confinement & Fusion Systems
Ghent University · 2025–Present

Dr. Gary S. Was
Radiation Materials & Structural Integrity
U. of Michigan · 2025–Present

Dr. Ray Sedwick
Direct Energy Conversion
U. of Maryland · 2025

OPERATIONS

Michael Laughlin
Chief Operating Officer
2022–Present

Martin Owens
Chief Strategy Officer
LANL / GE Hitachi · 2022–Present

MG (Ret.) Paul Pardew
Chief Contracting Officer
Army Contracting Command · 2022–Present

David Beck
Fusion Commercialization
U.S. Space Force · 2024–Present

Sushma Bhatia
Environmental & Legislative
Google · 2022–Present

Michael De Frenza
Technology Licensing
2023–Present

MG (Ret.) Robin L. Fontes
Cybersecurity & Defense
Army Cyber Command · 2022–Present

Vijay Gehani
Supply Chain & Components
INOX India · 2024–Present

Jon Michel Greenwood
IT & AI Infrastructure
Live Nation · 2023–Present

Brian C. O'Neill
National Security
CIA / ODNI · 2022–Present

Gen. (Ret.) Gustave F. Perna
DoD Liaison
Operation Warp Speed · 2022–2023

Andrea Romero
Marketing Lead
2022–Present

Legal counsel is retained; those roles are held on the internal roster and are not listed here.

SOURCES

References

1 H-S Bosch and G M Hale, Improved formulas for fusion cross-sections and thermal reactivities, *Nucl. Fusion* **32** 611 (1992). doi:10.1088/0029-5515/32/4/I07

2 W M Nevins and R Swain, The thermonuclear fusion rate coefficient for p–^{11}B reactions, *Nucl. Fusion* **40** 865 (2000). doi:10.1088/0029-5515/40/4/310

3 S V Putvinski, D D Ryutov and P N Yushmanov, Fusion reactivity of the pB^{11} plasma revisited, *Nucl. Fusion* **59** 076018 (2019). doi:10.1088/1741-4326/ab1a60

4 R M Magee *et al*, First measurements of p^{11}B fusion in a magnetically confined plasma, *Nat. Commun.* **14** 955 (2023). doi:10.1038/s41467-023-36655-1

5 W M Nevins, A review of confinement requirements for advanced fuels, *J. Fusion Energy* **17** 25 (1998). doi:10.1023/A:1022513215080

6 T H Rider, Fundamental limitations on plasma fusion systems not in thermodynamic equilibrium, *Phys. Plasmas* **4** 1039 (1997). doi:10.1063/1.872556

7 J D Lawson, Some criteria for a power producing thermonuclear reactor, *Proc. Phys. Soc. B* **70** 6 (1957). doi:10.1088/0370-1301/70/1/303

8 S E Wurzel and S C Hsu, Progress toward fusion energy breakeven and gain as measured against the Lawson criterion, *Phys. Plasmas* **29** 062103 (2022). doi:10.1063/5.0083990

9 G L Kulcinski and J F Santarius, Advanced fuels under debate, *Nature* **396** 724 (1998). doi:10.1038/25456

10 L J Wittenberg, J F Santarius and G L Kulcinski, Lunar source of ^{3}He for commercial fusion power, *Fusion Technol.* **10** 167 (1986).

11 M H Sikora and H R Weller, A new evaluation of the ^{11}B(p,α)$\alpha\alpha$ reaction rates, *J. Fusion Energy* **35** 538 (2016).

12 D A Brown *et al*, ENDF/B-VIII.0: the 8th major release of the nuclear reaction data library, *Nucl. Data Sheets* **148** 1 (2018). doi:10.1016/j.nds.2018.02.001

13 Y Xu, K Takahashi, S Goriely, M Arnould, M Ohta and H Utsunomiya, NACRE II: an update of the NACRE compilation of charged-particle-induced thermonuclear reaction rates for nuclei with mass number $A < 16$, *Nucl. Phys. A* **918** 61 (2013). doi:10.1016/j.nuclphysa.2013.09.007

14 R W Moir and W L Barr, “Venetian-blind” direct energy converter for fusion reactors, *Nucl. Fusion* **13** 35 (1973). doi:10.1088/0029-5515/13/1/005

15 R F Post, The magnetic mirror approach to fusion, *Nucl. Fusion* **27** 1579 (1987). doi:10.1088/0029-5515/27/10/001

16 T K Fowler, R W Moir and T C Simonen, A new simpler way to obtain high fusion power gain in tandem mirrors, *Nucl. Fusion* **57** 056014 (2017). doi:10.1088/1741-4326/aa5e54

17 D Endrizzi *et al*, Physics basis for the Wisconsin HTS Axisymmetric Mirror (WHAM), *J. Plasma Phys.* **89** 975890501 (2023). doi:10.1017/S0022377823000806

18 N J Fisch and J-M Rax, Interaction of energetic alpha particles with intense lower hybrid waves, *Phys. Rev. Lett.* **69** 612 (1992). doi:10.1103/PhysRevLett.69.612

19 M Abdou *et al*, Physics and technology considerations for the deuterium–tritium fuel cycle and conditions for tritium fuel self sufficiency, *Nucl. Fusion* **61** 013001 (2021). doi:10.1088/1741-4326/abbf35

20 J E Menard *et al*, Fusion nuclear science facilities and pilot plants based on the spherical tokamak, *Nucl. Fusion* **56** 106023 (2016). doi:10.1088/0029-5515/56/10/106023

21 B N Sorbom *et al*, ARC: a compact, high-field, fusion nuclear science facility and demonstration power plant with demountable magnets, *Fusion Eng. Des.* **100** 378 (2015). doi:10.1016/j.fusengdes.2015.07.008

22 A J Creely *et al*, Overview of the SPARC tokamak, *J. Plasma Phys.* **86** 865860502 (2020). doi:10.1017/S0022377820001257

23 R K Romano, N E Horelik, B R Herman, A G Nelson, B Forget and K Smith, OpenMC: a state-of-the-art Monte Carlo code for

COLOPHON

How this document was made

The Kronos Fleet — Combined Editorial, 2026 is set in **Fraunces** (display), **Gelasio** (text), and **IBM Plex Mono** (data & equations), carried forward from the Kronos editorial design system.

The figures are rendered at 300 dpi from the deposited generator scripts; the document is composed as a single self-contained file with embedded fonts and imagery, paginated to US Letter, and rendered to PDF through a headless Chromium engine in matched light and dark editions.

Every headline quantity carries an evidence class; withdrawn and restated values are marked as such. Nothing herein is frozen beyond the founder-approved Tier-A set.

Explore it live — turn the interactive 3-D model, run the deposited solvers in the physics validator, and watch the companion film series.

LEGAL NOTICE

Notice, status, and distribution

Conceptual design & simulation study. This document reports a conceptual design and simulation study. It is not a construction commitment, a safety-analysis report, a regulatory filing, or an offer of securities. Forward-looking statements — schedules, costs, market sizes, and performance — are estimates subject to the limitations set out in the Simulations part and may change.

Numbers and their classes. Quantities are reported with evidence classes and case labels; modelled, assumed, and requirement-class values are identified as such and are not to be quoted without their labels.

Public edition. This edition carries the physics and design only; all financial, funding, and defense-commercial content has been removed for public distribution. The scientific text corresponds to the arXiv and journal submissions.

THE 2026 KRONOS SERIES

One programme, many papers

This editorial is one paper in the Kronos 2026 series — a real fusion company's complete, reproducible physics record for a spherical-tokamak breeder and its low-neutron D–^{3}He tandem-mirror burners. Every headline number is a frozen anchor in the Physics De-Risking Register.

Explore the whole programme: the De-Risking Register, the interactive 3-D model, and the physics validator.

KRONOS FUSION ENERGY

An Advanced-Fuel Scorecard for D-T, D-D, D-3He and p-11B: Reactivity, Neutron Fraction and Direct-Conversion Trades Behind the Breeder and Burner Fuel Choices

A real fusion company building real machines. Explore the science, live.

Zenodo · doi:10.5281/zenodo.22645766

Read on kronosfusionenergy.com

The Physics De-Risking Register